ANALYSIS ON THERMAL AND HYDRAULIC PERFORMANCE OF A T-SHAPED VAPOR CHAMBER DESIGNED FOR MOTORCYCLE LED LIGHTS

Qifei JIAN*[1], Cong LI[1], Li WANG[2]

[*1]School of Mechanical and Automotive Engineering, South China University of Technology, Guangzhou 510640, Guangdong, China

[2]Haigang Jie, 234 Xing Gang East Road, Guangzhou, Guangdong, China

Abstract: Experiment and numerical analyses were conducted to study the thermal performance and circulation characteristic of the working fluid of a T-shaped vapor chamber special designed for the motorcycle LED light. The influences of heat loads and cooling magnitude were experimentally investigated. Results show that both the heat loads and cooling conditions have strong influences on the thermal performance of the vapor chamber, and the thermal resistance in the extended section occupies over 75.8% of the overall thermal resistance of the vapor chamber. Simulation results indicate that large pressure drop occurs along the extended section of the vapor chamber, and causes large temperature difference along the extended section.
Keywords: vapor chamber; pressure drop; heat transfer; thermal resistance; numerical analysis; heat conduction

Introduction

Vapor chamber (VC) has been an excellent candidate for solving the thermal management problems in many industries, such as electronic systems. VCs can swiftly spread heat from a hot spot to the surroundings. Studies of the influences of inner structure on the thermal performance of the VCs have been conducted by many researchers. Li Yong et al. [1] experimentally investigated the manufactured copper water vapor chambers with two wick structures. Their results showed that vapor chambers with copper foam wick structures exhibit good temperature uniformity and vapor chambers with copper powder exhibit low thermal resistance. A study conducted by M. Reyes et al. [2] was proposed on the behavior of a vertically placed vapor chamber based heat spreader intended for avionics applications. A mini-evaporator area made up of an array of mini-fin-pins was implemented for enhancing the boiling inside the vapor chamber. The experiment results showed that from the heat transfer standpoint, vapor chamber heat spreaders were always more efficient. Other studies focus on the effect of the wick structures could be seen in Ref. [3-10]. The vapor space height, evaporator section structure and the fill ratio of working fluid have also been considered in other studies. C.-K. Huang et al. [11] fabricated and tested the vapor chambers with five different vapor space heights. They found that the vapor chamber achieved the optimum design when the hydraulic diameter ratio was greater than 0.6. Te-En Tsai et al. [12] experimentally investigated the influence of heating power, fill ratio of working fluid, and evaporator surface structure on the thermal performance of a two-phase vapor chamber system for electronic cooling. The results suggested that either a growing heating power or a decreasing fill ratio decreased the overall thermal resistance, and the surface influenced the evaporator function prominently.

Numerical analysis is an effective method for analyzing the hydrothermal characteristics of the vapor chamber. In the study of Faghri et al. [13], the vapor core was treated as a single interface between the evaporator and condenser so as to avoid dealing with the two-phase problem, and only the heat conduction between each control volume is considered. Similar method is also seen in the studies of Chen et al. [14] and [15], and Lu et al. [16]. Their method (Ref. [13-16]) is very easy to use, very time efficient and agrees well with the experiment results. In the work of Vadakkan et al. [17], a three dimensional model to analyze the transient and steady-state performance of flat heat pipes subjected to heating with discrete heat sources is proposed. Vapor flow, temperature and hydrodynamic pressure fields are computed from coupled continuity/momentum and energy equations in the wick and vapor regions. Their analysis highlights the importance of considering axial diffusion through the wall and wick in determining the temperature distribution in flat heat pipes.

Above all, the influences of VC inner structures on thermal performance of VCs have been studied by many researchers. Since the outer shape of VCs must fit the components that need heat dissipation, the outer shape thus may also influence the heat transfer performance of VCs. However, studies as stated above rarely considered the influences of the outer shape of VCs. In this paper, the thermal performance of a T-shaped vapor chamber (TSVC) special designed for the thermal management of motorcycle high power LED lights was studied experimentally. The influences of heat loads and cooling capability of heat sink were considered. Numerical model has also been proposed based on FLUENT [16, 18, 19], to investigate the thermal hydrodynamic characteristics of the working fluid inside the TSVC. The results obtained in this paper could provide references on improving the thermal performance of this T-shaped vapor chamber.

Thermal performance test

Thermal performance apparatus is shown in fig. 1. The apparatus for thermal performance test were established for studying the thermal performance of this T-shaped VC. The photograph of the TSVC is shown in fig. 2. Fig. 2(b) shows the operating mechanism of the TSVC. The TSVC is made of copper and de-ionized water is used as the working fluid.

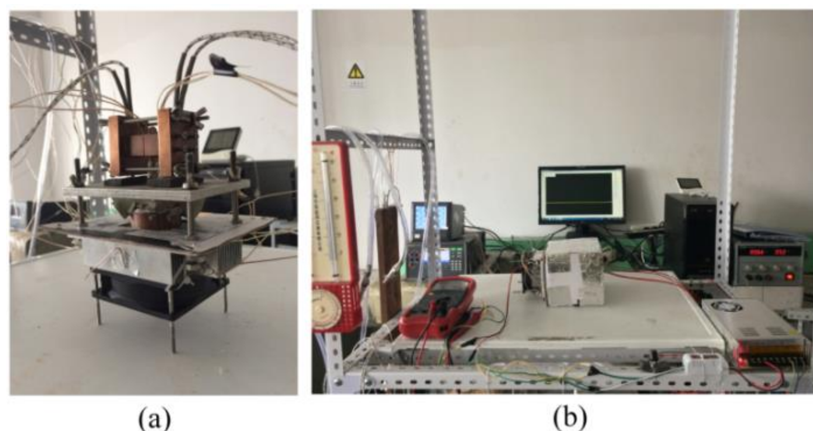

(a) (b)

Fig. 1 Experiment apparatus for testing the T-shaped VC

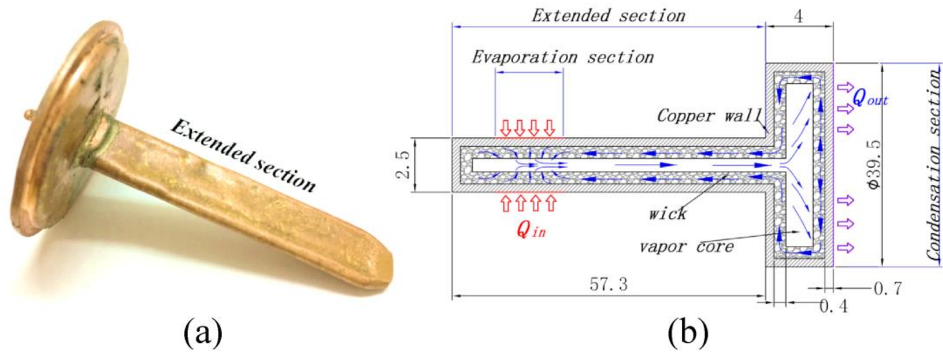

Fig. 2 Schematic diagram of the T-shaped vapor chamber

In the thermal performance test, two rod heaters embedded in the copper heating blocks (as shown in fig. 3a) were used as the heating sources. Heat was transferred through the heat conduction blocks to the evaporation section of the TSVC. Thermal silicone grease was applied between the heat conduction block and the TSVC evaporation section to remove the air gap. Thermal conductivity of the thermal silicone grease is $2.0\ \mathrm{W/m\cdot K}$. Heating power of the rod heaters were varied by DC power supply (ATTEN TPR3020S). The voltage applied on the rod heater was ranging from 5V to 14V in 3V increments. As shown in fig. 3, the evaporation section was located at both sides of the extended section. The heating area was $12.5\mathrm{mm} \times 15\mathrm{mm}$ on each side of the extend section. The condensation section was cooled by the heat sink with air fan. The fan speed was controlled by voltage regulator and DC converter to vary the cooling air flow rate. The voltage applied on the fan was increased from 5V to 17V in 3V increments. The ambient temperature is about $298 \pm 1.5\mathrm{K}$. 19 OMEGA K-type thermocouples (defined as $T_1 \sim T_{19}$) and FLUKE 2638A digital data logger were used to measure the temperature at different positions. Detailed location of thermocouples was also illustrated in fig. 3.

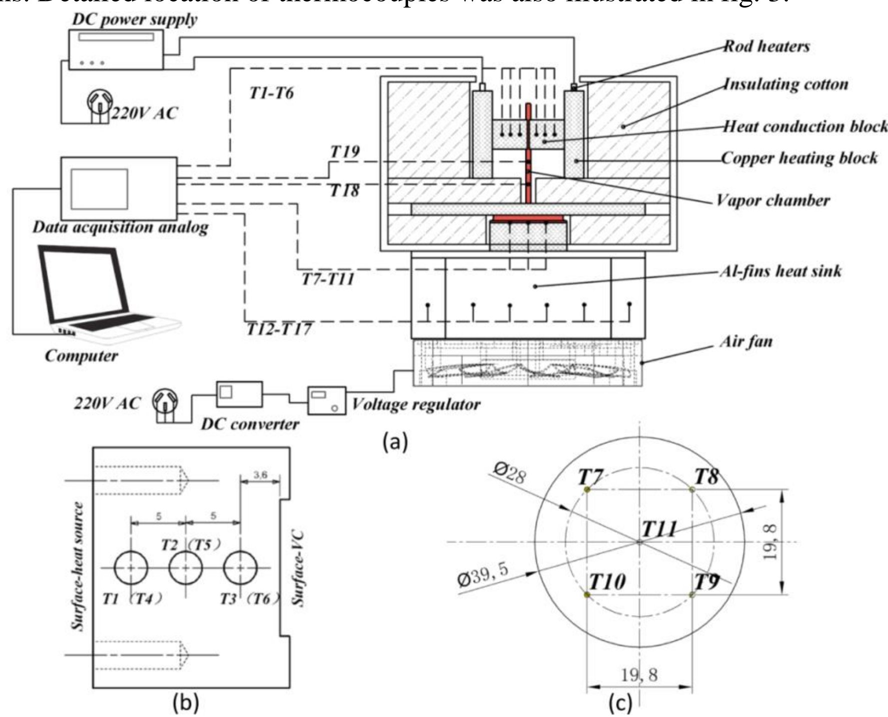

Fig. 3 Schematic diagram of the thermal performance of T-shaped VC

Based on energy conservation and Fourier heat conduction law, the temperature of evaporation section of TSVC contacted with the heat conduction block is calculated and expressed as follows:

$$T_h = 0.5\{[T_3 - (h_{3-h}/h_{2-h})(T_2 - T_3)] + [T_2 - (h_{2-h}/h_{1-2})(T_1 - T_2)]\} \quad (1)$$

In eq. 1, h_{i-j} is the length between the measurement point i and j, $i = 1,2,3$; $j = 2, \mathrm{h}$.The subscript h refers to the surface between the copper heating block and vapor chamber, as shown in fig. 3. The temperature of condensation section surface of the VC is set as the average temperature of the five thermal couples located at the interface between the heat sink and VC, and is calculated as follows:

$$T_c = 0.2(T_7 + T_8 + T_9 + T_{10} + T_{11}) \quad (2)$$

The overall thermal resistance (R_{VC}) of TSVC is determined using the expression as follows.

$$R_{VC} = (T_h - T_c)/\mathrm{Q} \quad (3)$$

Equivalent heat transfer coefficient of the heat sink k_c is calculated based on the temperature difference between the temperature of the condensation section surface of VC and the ambient.

$$k_c = \mathrm{Q}/[A_c \cdot (T_c - T_\infty)] \quad (4)$$

Uncertainty analysis

The measurement error of the temperature data logger is 0.6K as presented in the manufacturer instructions, while the measurement error of the thermal couples is 0.2K. Assume that the uncertainties of data obey uniform distribution, the coverage factor K is $\sqrt{3}$. Then the uncertainties of the temperature data acquisition instrument and the thermal couples are 0.346K, 0.1155K respectively. According to the manufacturer instruction of DC power supply, the measurement errors of current and voltage are 0.5%rdg+0.02A and 0.5%rdg+0.2V respectively.

The uncertainty of the temperature data directly measured by FLUKE 2638A digital data logger using thermal couples is 0.365K. Uncertainties of the current and voltage applied on the rod heaters are listed in table 1. The maximum uncertainty of the heating power applied on the evaporation section is 1.5095W. Uncertainty of the overall thermal resistance of the T-shaped vapor chamber (TSVC) is shown in fig. 4. The maximum uncertainty of the overall thermal resistance is 0.35K/W as the heat load of 3.3w and fan voltage of 17V.

Table 1 Uncertainties of the current, voltage and power applied on the rod heaters

Current/ A	Error/ A	Uncertainty/ A	Voltage/ V	Error/ V	Uncertainty/ V	Power/ W	Uncertainty/ W
0.66	0.0233	0.01345	5	0.225	0.1299	3.30	0.6359
1.06	0.0253	0.01461	8	0.240	0.1386	8.48	1.0605
1.44	0.0272	0.01570	11	0.255	0.1472	15.84	1.5095

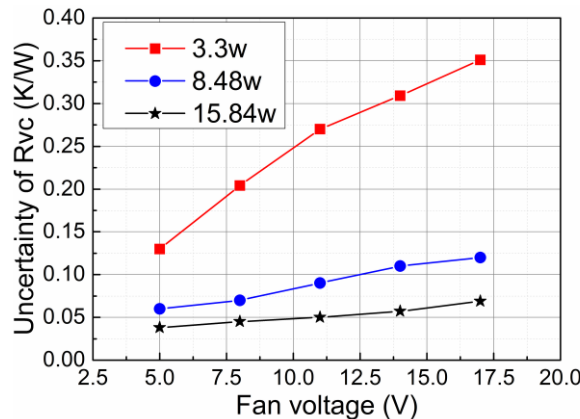

Fig. 4 Uncertainty of the overall thermal resistance of T-shaped VC versus fan voltage

Physical model

A two dimensional physical model was developed to investigate the thermal hydrodynamic characteristics of the working fluid inside the VC. As shown in fig. 2(b), the TSVC was divided into three sections, including extended section, evaporation section and condensation section. Sintered copper powder layer forms the wick structure of this vapor chamber. The copper powder has a diameter of about 141μm. Heat load is applied on the evaporation section, which is 15mm long in 2D model. The condensation section has a diameter of 39.5mm. Except the evaporation section and condensation section, all other outer walls are assumed adiabatic. For simplifying the model, the heat sink of the VC is equivalent to a convective heat transfer coefficient applied on the condensation section, and the equivalent convective heat transfer coefficient is calculated based on eq. 4. Thicknesses of copper wall and wick structure are 0.7mm and 0.4mm respectively. The thermo-physical properties of the copper wall and wick are given in table 2. The effective thermal conductivity of the wick structure is determined based on Maxwell's equation [20], expressed in eq. 5. The boundary conditions are determined according to the experiment setup. The initial temperature all through the vapor chamber and ambient temperature are set as 298K.

$$k_{wick} = k_{wall}\{[2 + k_l/k_{wall} - 2\varepsilon(1 - k_l/k_{wall})]/[2 + k_l/k_{wall} + \varepsilon(1 - k_l/k_{wall})]\} \quad (5)$$

Table 2 Thermo physical properties of the VC material and working fluid

Copper	Thermal conductivity	387.6W/m K
	Specific heat	381J/kg K
	Density	8978kg/m^3
Wick	Thermal conductivity	104.874 W/m K
	Porosity	0.644
	Permeability	2.67×10^{-11}m^2
Water	Thermal conductivity	0.6 W/m K
	Specific heat	4182 J/kg K
	Density	984.645 Kg/m^3
	Viscosity	0.000493 N s/m^2
Water vapor	Thermal conductivity	0.0261 W/m K
	Specific heat	2014 J/kg K
	Density	0.116 kg/m^3
	Viscosity	1.34×10^{-5}N s/m^2
Water/vapor	Latent heat of vaporization	2364.89 kJ/kg

Mathematical model and governing equations

According to the FHP network model proposed by Faghri [13], the liquid return process in the wick is extremely important to the working fluid circulation, while it has little effect on the heat transfer, thus neglecting the liquid-vapor interfacial convective heat exchange, and assuming that evaporation and condensation of the working fluid take place smoothly at the wick-vapor interface. As stated in the network model of Faghri [13], the vapor flow thermal resistance is considerably smaller than the other

processes inside the heat pipe, thus the vapor core is treated as a constant temperature interface. Other assumptions are listed as followings, as also stated in Ref. [21]:

1) A steady-state condition is established.
2) Laminar flow in both the vapor core and wick section.
3) The wick structure is isotropic and fully saturated.
4) The gravity influence is negligible.

Similar assumptions could also be found in Refs. [15] and [16] and the validity was confirmed. The energy balance at the interface is then obtained based on the energy conservation and Fourier heat conduction law, as shown in eq.6. The users-define functions (UDFs) were used to define the boundary conditions and source terms.

$$Q_e = \sum_{i}^{e-wick} \left[\frac{k_i A_i}{\Delta L/2}(T_i - T_v)\right] = Q_c = \sum_{i}^{c-wick} \left[\frac{k_i A_i}{\Delta L/2}(T_v - T_i)\right] \quad (6)$$

Thus, the vapor core temperature is then determined as follows:

$$T_v = \sum_i \frac{k_i A_i}{\Delta L} T_i)/\left(\sum_i \frac{k_i A_i}{\Delta L}\right) \quad (7)$$

T_i is the interface temperature, and ΔL represents the length of each grid cell. The subscript i represents the wick-vapor interface. The vapor core temperature T_v is determined using the Users Defined Function (UDFs). Ignoring the liquid flow in tangential direction [17], then the mass conservation at each face of the liquid-vapor interface is determined as follows:

$$m_i = [k_i A_i (T_i - T_v)]_{e-wick}/(h_{fg}\,\Delta L/2) = [k_i A_i (T_v - T_i)]_{c-wick}/(h_{fg}\,\Delta L/2) \quad (8)$$

$$V_{normal,l} = m_i/(\rho_l A_l), V_{normal,v} = m_i/(\rho_v A_v) \quad (9)$$

The continuity, momentum equations for wick region and vapor core and energy equation for the solid wall and wick region, and the vapor core are list as follows:

$$\varepsilon \frac{\partial \rho}{\partial t} + \nabla \cdot (\rho \cdot \vec{V}) = 0 \quad (10)$$

$$\rho \vec{V} \cdot \nabla \vec{V} = -\varepsilon \nabla p + \mu \nabla^2 \vec{V} + S_D \quad (11)$$

$$\nabla^2 T = 0 \quad (12)$$

Details boundary conditions are listed in table 3. Users Defined Function (UDFs) is used to calculate the local mass flux at each grid face of the interface based on eq. 5. The normal velocity at each face of the interface is then obtained in eq. 6, and stored as a boundary file. The SIMPLE algorithm and control volume method are employed to solve the governing equations using FLUENT 6.3.Convergence of the energy equation is estimated as relative error between the heat input at evaporator wall and the heat output at condenser wall is within $\pm 0.05\%$.

Table 3 Boundary conditions of the numerical model

Wick-vapor interface	$\rho_l \vec{V_l} = \rho_v \vec{V_v}$
	$T = T_v = T_{sat}$
Evaporation section	$k_{wall}(\partial T/\partial y) = q$
Condensation section	$-k_{wall}(\partial T/\partial y) = k_c(T_c - T_\infty)$
Adiabatic walls	$k_{wall}(\partial T/\partial y) = 0$
Solid wall-wick region interface	$k_{wall}(\partial T_{wall}/\partial n) = k_{wick}(\partial T_{wick}/\partial n)$
	$v = u = 0$

Mesh independence and numerical model validation

Before the simulation analysis, mesh independence needed to be demonstrated by comparing the results in different mesh numbers. Five mesh numbers (22060, 26696, 29482, 40200, and 58714) were tested and compared. The heat flux was set as $2000W/m^2$ on each side of the evaporation section. The equivalent convective heat transfer coefficient at the condensation section and the ambient temperature were set as $200W/(m^2 \cdot K)$ and 298K, respectively. Based on the comparisons results, the mesh number of 40200 was selected for numerical calculation.

In order to validate the numerical model, the simulation results were compared with the experiment conducted in this paper. Fig.5 shows the comparisons of the evaporation section temperature of the numerical results and experiment results in this paper. It can be seen the maximum relative error of the simulation result with the experiment results in this paper is less than 1%. Therefore, the simplified numerical model proposed in this paper could be considered reliable.

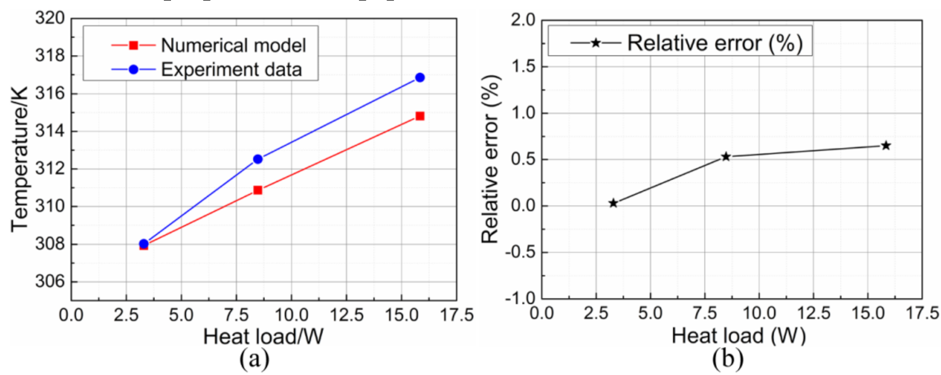

Fig. 5 Model validation with the experiment results in this paper

Results and discussion

Fig. 6 shows the velocity and pressure distribution of the TSVC as the heat load is 15.84W, and the cooling fan voltage is 11V. The circulation of the working fluid inside the TSVC is shown in fig. 6(a). Fig. 6(c) illustrates the pressure variation inside the vapor core. A-B section refers to the evaporation section, while D-E section refers to the bottom space between the outlet of extended section and condensation section. Pressure drop along the extended section is considered to include two parts (ΔP_{A-B} & ΔP_{B-D}). The pressure drop ΔP_{A-B} represents the pressure loss of the fluid at the evaporation section, while ΔP_{B-D} is the pressure drop vapor flowing along the extended section.

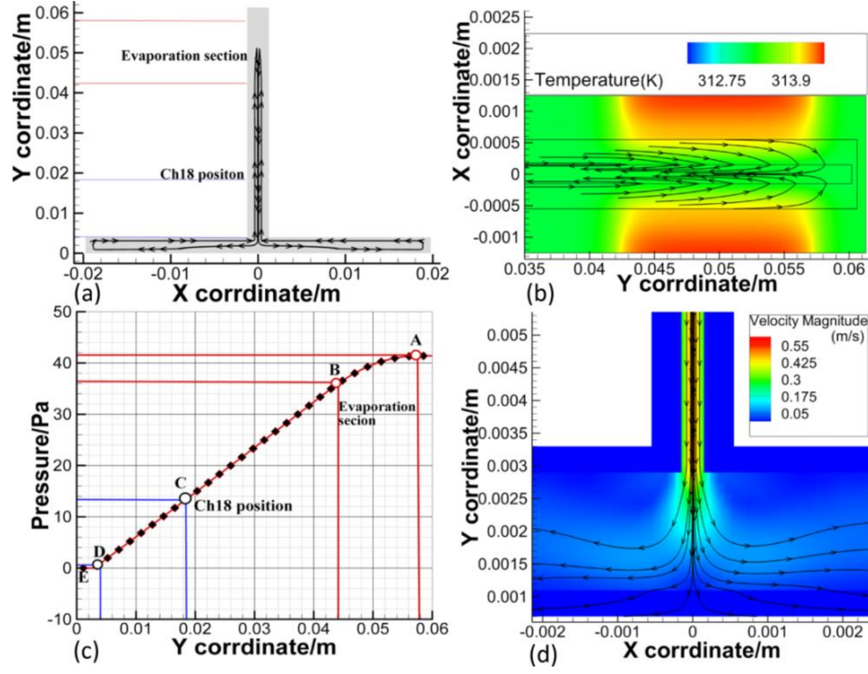

Fig. 6 Velocity distribution of the working fluid in the T-shaped VC: (a) Circulation of the fluid in T-shaped VC; (b) Fluid velocity distribution at evaporation section; (c) Pressure variation in vapor core; (d) Fluid velocity distribution at condensation section

Because of the symmetrically located heat sources, the vapor flows into the vapor core in opposite direction at the evaporation section, shown in fig. 6(b). The opposite direction flow could cause large pressure loss, represented by ΔP_{A-B}. The second part of pressure loss ΔP_{B-D} is caused by the effect of shear stress at the wick-vapor interface along the extended section and high vapor velocity. When the vapor velocity is sufficient to entrain liquid returning to the evaporation section, the thermal performance and evaporation in the evaporator will decline. And the shear stress at the wick-vapor interface could hinder the flow of working fluid flowing to the evaporation section, worsen the evaporation progress in the wick and cause dry-out situation. Fig. 6(c) indicates that the pressure drop between the evaporation section and Ch18 location (represented by $\Delta \mathrm{P_{A-D}}$) is much larger than that between the location of Ch18 and the condensation section (represented by $\Delta \mathrm{P_{D-E}}$).

Ch18 and Ch19 (corresponding to T18 &T19) were the data acquisition channels of two thermal couples located at the extended section, as shown in fig. 3. The overall thermal resistance of the TSVC is considered to be divided into two parts: the thermal resistance between the evaporation section and ch18, and the thermal resistance between ch18 and the condensation section.

$$R_{Th-Tch18} = (T_h - T_{ch18})/\mathrm{Q} \quad (13)$$

$$R_{Tc-Tch18} = (T_{ch18} - T_c)/\mathrm{Q} \quad (14)$$

Variation of the ratio $R_{Th-Tch18}/R_{VC}$ and $R_{Tc-Tch18}/R_{VC}$ versus heat loads and fan voltages is shown in fig. 7. The thermal resistances $R_{Th-Tch18}$ and $R_{Tc-Tch18}$ are defined and expressed in eq. 13 and 14. $R_{Th-Tch18}$ is the thermal resistance between the evaporation section of the T-shaped VC and the location of ch18, while $R_{Tc-Tch18}$ is the thermal resistance between the condensation section of the TSVC and the location of ch18. It can be observed from fig. 7 that the thermal resistance ($R_{Th-Tch18}$) between the evaporation section and ch18 occupies more than 60% of the overall thermal resistance ($\mathrm{R_{VC}}$). And the proportion of $R_{Th-Tch18}$ increases with the increase of heat loads. When the heat load is 15.84W, the proportion of $R_{Th-Tch18}$ is in the range of 75.8%~92.4% for different cooling fan

voltages, while $R_{Tc-Tch18}$ takes over only 7.59%~24.18%. The extended section of the TSVC is considered to contribute the main thermal resistance proportion to the overall thermal resistance of the TSVC.

$$\Delta \ln P / \Delta T = h_{fg} / (R_{gas} T^2) \quad (15)$$

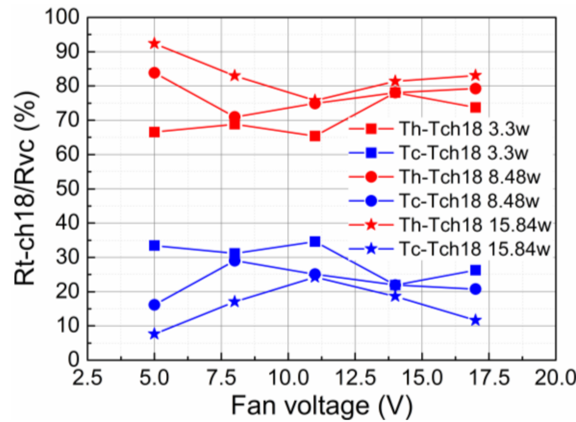

Fig. 7 Variation of ratio $R_{Th-Tch18}/R_{VC}$ and $R_{Tc-Tch18}/R_{VC}$ with different heat loads and fan voltages

Since the thermal resistance could be represented by temperature difference, and according to the Clausius-Clapeyron equation (eq. 15), the large pressure drop could result in large temperature differences, similar results could also be seen in fig. 6. Since ΔP_{A-C} is higher than ΔP_{C-E} as shown in fig. 6(c), the temperature difference $\Delta T_{Th-Tch18}$ is then larger than $\Delta T_{Tc-Tch18}$ based on the Clausius-Clapeyron equation. ΔP_{D-E} is the pressure drop from the outlet of the extended section to the condensation section, and is much small as compared to ΔP_{A-D}, as shown in fig. 6(c), which causes much smaller temperature difference than in the extended section.

The thermal performance of the TSVC was experimentally investigated by applying various heat loads and cooling conditions (varied by the fan voltages). Temperature difference between the evaporation section and condensation section is shown in fig. 8(a). It can be seen that the temperature difference increases with the increase of cooling fan voltage and heat load. When the voltage applied on the rod heaters is 11V, the heat load reaches 15.84W, and with the fan voltage of 5V, the temperature difference between the evaporation and condensation section of the TSVC is 6.35K. However, as the fan voltage is 17V, the temperature difference reaches 11.44K.

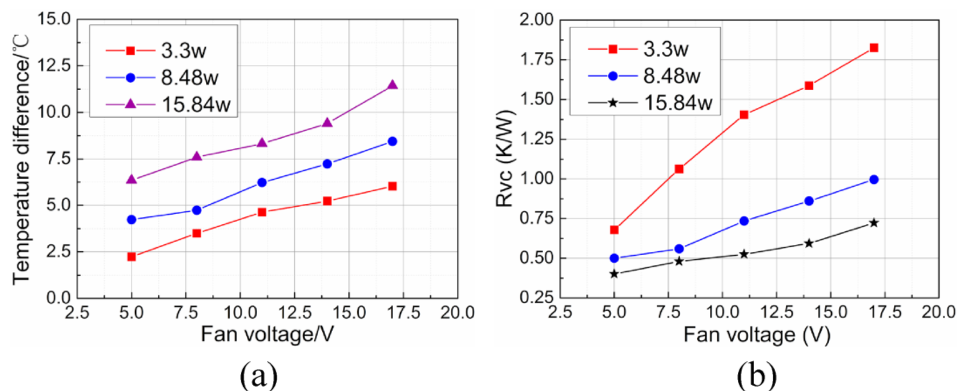

Fig. 8 Temperature difference between the evaporation condensation section (a) and variation of the overall thermal resistance of T-shaped VC (b) versus different heat loads and fan voltages

Variation of the overall thermal resistance (R_{VC}) of the TSVC versus heat loads and cooling fan voltages are illustrated in fig. 8(b). The overall thermal resistance of this T-shaped VC increases with the increase of cooling fan voltages. However, as the heat loads increases, the overall thermal resistance decreases. When the voltage applied on the rod heaters is 5V, the heat load is 3.3W, and the overall thermal resistance of the TSVC is ranging from $0.679\text{K/W}\sim1.826\text{K/W}$, which is much higher than in the other two heat loads conditions. The overall thermal resistance reaches the minimum value in all these three heat loads conditions when then cooling fan voltage is 5V. And the minimum thermal resistances of the TSVC corresponding to the heat load of 3.3W, 8.48W and 15.84W are 0.679K/W, 0.499K/W, and 0.401K/W, respectively.

Conclusions

Both experiment and numerical analysis were conducted to investigate the heat transfer performance of a T-shaped vapor chamber (TSVC) designed for the thermal management of motorcycle high power LED lights. The influences of heat loads and cooling conditions on the thermal performance of the TSVC were investigated experimentally. Results indicate that both the heat loads and cooling magnitude have strong influences on the thermal performance of the TSVC, and the thermal resistance in the extended section occupies most proportion of the overall thermal resistance of the TSVC. When the heat load is 15.84W, the proportion of $R_{Th-Tch18}$ in the overall thermal resistance of the TSVC is in the range of $75.8\%\sim92.4\%$ for different cooling fan voltages, while $R_{Tc-Tch18}$ takes over only $7.59\%\sim24.18\%$.

Experiment results also suggest that the overall thermal resistance of the TSVC increases with the increase of heat loads and cooling fan voltage. The minimum thermal resistances of the TSVC are 0.679K/W, 0.499K/W, and 0.401K/W corresponding to the heat loads of 3.3W, 8.48W, and 15.84W and the cooling fan voltage is 5V, respectively. The proposed numerical model was validated by comparing with the experiment results. The circulation characteristic of working fluid inside this TSVC was obtained according to the simulation results. And the results indicate that large pressure drop occurs along the extended section of the TSVC, which causes large temperature difference. Thus the design of the extended section of this T-shaped vapor chamber plays an important role in enhancing the thermal performance of this TSVC.

Acknowledgment

This research were supported by the Guangdong Province Science and Technology Program (No.2016B090918034), the Guangzhou Science and Technology Program (No. 201508010045), and the Guangzhou Nan -Sa District Science and Technology Program (No. 2015CX001)

Nomenclature

A	Area [m2]	***Greek***	
h	Distance [m]	ε	Wick porosity
h_{fg}	Latent heat of vaporization [kjkg-1]	λ	Thermal conductivity [Wm-1K-1]
k	Thermal conductivity [Wm-1K-1]	ρ	Density [kgm-3]
k_c	Convective heat transfer coefficient	***Subscript***	

	[Wm-2K-1]		
ΔL	Side length of a control volume [m]	*c*	Condensation section
m_i	Mass flux [kgs-1]	*e*	Evaporation section
p	Pressure [pa]	*i*	Wick-vapor interface
Q	Heat transfer rate [W]	*l*	Liquid region
q	Heat flux [Wm-2]	*normal, l*	Normal direction in liquid interface
R_{gas}	Gas constant	*normal, v*	Normal direction in vapor interface
R	Thermal resistance [KW-1]	*sat*	saturation
T	Temperature [K]	*v*	Vapor region
u_c	The uncertainty	*wall*	Solid wall
$\vec{V}$	Velocity vector [ms-1]	*wick*	Wick structure
		∞	ambient

References

[1] Y. Li, et al., Experimental investigation of vapor chambers with different wick structures at various parameters Experimental Thermal and Fluid Science, 77 (2016) 132-143.

[2] M. Reyes, et al., Experimental and theoretical study of a vapour chamber based heat spreader for avionics applications Applied Thermal Engineering, 37 (2012) 51-59.

[3] W. Mengyao, et al., Experimental characterization of Si micropillar based evaporator for advanced vapor chambers 2014 IEEE 16th Electronics Packaging Technology Conference (EPTC), (2014) 335-340.

[4] Y. Peng, et al., A novel wick structure of vapor chamber based on the fractal architecture of leaf vein International Journal of Heat and Mass Transfer, 63 (2013) 120-133.

[5] S. Zhen and Q. Huihe, An asymmetrical vapor chamber with multiscale micro/nanostructured surfaces International Communications in Heat and Mass Transfer, 58 (2014) 40-44.

[6] S. Sprinceana, et al., Capillary layer structure effect upon heat transfer in flat heat pipes, in: 7th International Conference on Advanced Topics in Optoelectronics, Microelectronics, and Nanotechnologies (ATOM-N), Vol. 9258, Constanta, ROMANIA, 2014.

[7] X. Ji, et al., A vapor chamber using extended condenser concept for ultra-high heat flux and large heater area International Journal of Heat and Mass Transfer, 55 (2012) 4908-4913.

[8] J.A. Weibel, et al., Design of Integrated Nanostructured Wicks for High-Performance Vapor Chambers Ieee Transactions on Components Packaging and Manufacturing Technology, 1 (2011) 859-867.

[9] J.A. Weibel, et al., Experimental Characterization of Capillary-Fed Carbon Nanotube Vapor Chamber Wicks Journal of Heat Transfer-Transactions of the Asme, 135 (2013) 7.

[10] Y.S. Ju, et al., Planar vapor chamber with hybrid evaporator wicks for the thermal management of high-heat-flux and high-power optoelectronic devices International Journal of Heat and Mass Transfer, 60 (2013) 163-169.

[11] C.K. Huang, et al., THE EFFECTS OF VAPOR SPACE HEIGHT ON THE VAPOR CHAMBER PERFORMANCE Experimental Heat Transfer, 25 (2012) 1-11.

[12] T.-E. Tsai, et al., Two-phase closed thermosyphon vapor-chamber system for electronic cooling International Communications in Heat and Mass Transfer, 37 (2010) 484-489.

[13] Z.J. Zuo and A. Faghri, A network thermodynamic analysis of the heat pipe International Journal of Heat and Mass Transfer, 41 (1998) 1473-1484.

[14] Y.-S. Chen, et al., Numerical simulation of a heat sink embedded with a vapor chamber and calculation of effective thermal conductivity of a vapor chamber Applied Thermal Engineering, 29 (2009) 2655-2664.

[15] Y.-S. Chen, et al., A simplified transient three-dimensional model for estimating the thermal performance of the vapor chambers Applied Thermal Engineering, 26 (2006) 2087-2094.

[16] L. Longsheng, et al., Numerical analysis on thermal hydraulic performance of a flat plate heat pipe with wick column Heat and Mass Transfer, 51 (2015) 1051-1059.

[17] U. Vadakkan, et al., Transport in flat heat pipes at high heat fluxes from multiple discrete sources Journal of Heat Transfer-Transactions of the Asme, 126 (2004) 347-354.

[18] K. Karabulut, et al., NUMERICAL INVESTIGATION OF THE EFFECT OF INSULATION ON HEAT TRANSFER OF THERMAL BRIDGES WITH DIFFERENT TYPES Thermal Science, 20 (2016) 185-195.

[19] K. Arslan, THREE-DIMENSIONAL COMPUTATIONAL FLUID DYNAMICS MODELING OF TiO2/R134a NANOREFRIGERANT Thermal Science, 21 (2017) 175-186.

[20] M.J. C., A Treatise on Electricity and Magnetism, Clarendon Press, 1954.

[21] Y. Koito, et al., Fundamental experiments and numerical analyses on heat transfer characteristics of a vapor chamber - (Effect of heat source size) Jsme International Journal Series B-Fluids and Thermal Engineering, 49 (2006) 1233-1240.